Laser and Particle Beams (2005), *23*, 275–282. Printed in the USA.

DOI: 10.1017/S026303460505038X

Study on two-dimensional transfer of radiative heating wave

KE LAN, TINGGUI FENG, DONGXIAN LAI, YAN XU, AND XUJUN MENG
Institute of Applied Physics and Computational Mathematics, Beijing, China
(RECEIVED 10 May 2004; ACCEPTED 12 December 2004)

Abstract

A two-dimensional (2D) multigroup radiation transfer hydrodynamics code LARED-R-1 is used to simulate a supersonic wave experiment performed earlier by the Livermore group. The main result is that, contrary to the conclusion of Back *et al.* (2000*a*), the average-atom opacity model is sufficient to explain the obtained experimental results, provided that an adequate description of the radiation transport was used. The simulation results from LARED-R-1 show the spectrum of radiation in foam with radius and length of several optical depths is not in Planckian distribution and the angular intensity distribution is anisotropic.

Keywords: Anisotropic; 2D multigroup radiation transfer; Radiatively heated foam; Supersonic wave

1. INTRODUCTION

The study of supersonic heat wave propagation in matter driven by thermal radiation is important for many fields, such as inertial confinement fusion (Borisenko *et al.*, 2003), Z-pinch (Chaikovsky *et al.*, 2003), and heavy ion driven fusion (Barnard *et al.*, 2003; Niemann *et al.*, 2003). After the first work done by Marshak (1958), theoretical (Zel'dovich & Raizer, 1966; Kaiser *et al.*, 1989), and experimental studies (Sigel *et al.*, 1990; Schwanda & Eidmann, 1992) were done extensively on this subject. Low-density material foam (Basko & Meyer-ter-Vehn, 1993; Borisenko *et al.*, 2003; Philippe *et al.*, 2004) has come to play an important role as an efficient converter and hence, many experiments were done on supersonic heat wave propagation in foam (Afshar-rad *et al.*, 1994; Massen *et al.*, 1994; Back *et al.*, 2000*a*, 2000*b*). Usually, it was assumed that the photons begin to thermalize at about one optical depth, that is, the emission is isotropic and the spectrum is in planckian distribution, so the diffusive approximation begins to be applicable. The diffusive approximation was therefore used very often to simulate the transfer process of supersonic wave in foam which is longer than one optical depth (Back *et al.*, 2000*a*, 2000*b*). However, it is necessary to investigate this fundamental assumption closely by using a detail simulation tool which can give the spectrum and the angular intensity distribution in radiation transfer, such as a two-dimensional (2D) multigroup radiation transfer hydrodynamics code.

In this paper, we used LARED-R-1, a 2D multigroup radiation transfer hydrodynamics code, to simulate the supersonic wave in a radiatively heated SiO_2 foam cylinder with radius and length of several optical depths, in order to study the spectrum and the angular intensity distribution in radiation transfer in this kind of foam. A S-N discrete ordinates method (Lewis & Miller, 1984; Menart, 2000) is used in LARED-R-1 to solve the radiative equation of transfer, so the spectrum and the angular intensity distribution can be obtained in the whole foam. In Section 2, we will introduce the model used in our simulation, and then compare the simulation results of LARED-R-1 with observations in Section 3. In Section 4, we will discuss the spectral distribution and the angular distribution of radiation in the SiO_2 foam cylinder because they are of fundamental interest in the study of supersonic propagation. Finally, a conclusion will be presented in Section 5.

2. CODE AND MODEL

In LARED-R-1, hydrodynamic equations are coupled to radiation transfer equation. The methods used in the code are discussed in other papers (Feng, 1995; Feng *et al.*, 1999, 2001). The equations of electron temperature T_e and ion temperature T_i in 2D cylindrical coordinate are:

Address correspondence and reprint requests to: Ke Lan, Institute of Applied Physics and Computational Mathematics, P.O. Box 8009-12, Beijing 100088, China. E-mail: lan_ke@iapcm.ac.cn

$$C_{ve}\frac{dT_e}{dt} = -T_e\left(\frac{\partial P_e}{\partial T_e}\right)_\rho \frac{d}{dt}\left(\frac{1}{\rho}\right) - \frac{1}{\rho R}\frac{\partial}{\partial R}(RF_{e,R}) - \frac{1}{\rho}\frac{\partial}{\partial Z}F_{e,Z} + W_{ie} + W_{re}, \quad (1)$$

$$C_{vi}\frac{dT_i}{dt} = -(P_i + q)\frac{d}{dt}\left(\frac{1}{\rho}\right) - \frac{1}{\rho R}\frac{\partial}{\partial R}(RF_{i,R}) - \frac{1}{\rho}\frac{\partial}{\partial Z}F_{i,Z} - W_{ie}. \quad (2)$$

In the above equations, t is time, C_{ve} and C_{vi} are respective specific heat of electron and ion, P_e is electron pressure, P_i is ion pressure, q is artificial viscosity, R is spatial position, ρ is mass density, $F_{e,R}$ and $F_{e,Z}$ are electron energy fluxes due to thermal conduction in radial direction and axial direction, respectively, $F_{i,R}$ and $F_{i,Z}$ are energy fluxes for ion, W_{ie} is electron-ion energy exchange, and W_{re} is electron-photon energy exchange.

The 2D radiation transfer equation is:

$$\frac{1}{c}\frac{dI_\nu}{dt} + \frac{\sin\theta\cos\omega}{R}\frac{\partial(RI_\nu)}{\partial R} + \cos\theta\frac{\partial I_\nu}{\partial Z} - \frac{1}{R}\frac{\partial(\sin\theta\sin\omega I_\nu)}{\partial\omega} = \mu'_\nu(B_\nu - I_\nu) + S_\nu - \sigma_{th}I_\nu + \frac{3\sigma_{th}}{16\pi}\int d\vec{\Omega}'[1 + (\vec{\Omega}\cdot\vec{\Omega}')^2]I_\nu(\vec{\Omega}'). \quad (3)$$

Here, I_ν is the specific intensity of radiation at radial position R and axial position Z, traveling in direction $\mathbf{\Omega}$, with frequency ν and at time t. The directional coordinate system is shown in Figure 1. As shown, θ is the angle of $\mathbf{\Omega}$ with $\mathbf{Z}$ axis and ω is that with the radial direction $\mathbf{R}$. The symbols u is plasma velocity, μ'_ν is effective absorption coefficient, B_ν is planckian function, S_ν is source function, and σ_{th} is Thomson scattering absorption coefficient.

The model used in our simulation is chosen from the experiment done by Back *et al.* (2000*a*). According to their experiments, a SiO_2 foam cylinder of 3 mm diameter and 10 mg/cm^3 density was cast into a 25 μm thick Au ring of three different lengths: 0.5, 1.0, and 1.5 mm. Figure 2 is a schematic of the SiO_2 foam and the Au ring. The X-ray radiation wave propagates axially down the cylindrical foam and finally breaks out of the exterior face. We define six characteristic positions in the figure, which are denoted by O_i and E_i $(i = 1,3)$. O_1 and E_1 are in the middle of the foam cylinder; O_3 and E_3 are on the exterior face; and O_2 and E_2 are 50 μm axially away from the exterior face. O_i $(i = 1,3)$ are on the axis of the foam cylinder, while E_i $(i = 1,3)$ are at the edge. The simulation results at these characteristic positions will be presented in Sections 3 and 4.

The X-ray driven temperature used in our simulation is fitted from the measured T_r (Back *et al.*, 2000*a*), as shown in Figure 3. In this simulation, an averaged atom model is used to supply opacities, and S-4 method (three discrete directions per octant) is used to solve the radiative equation of transfer. There are 100 frequency groups used, from 0 to 3×10^4 eV.

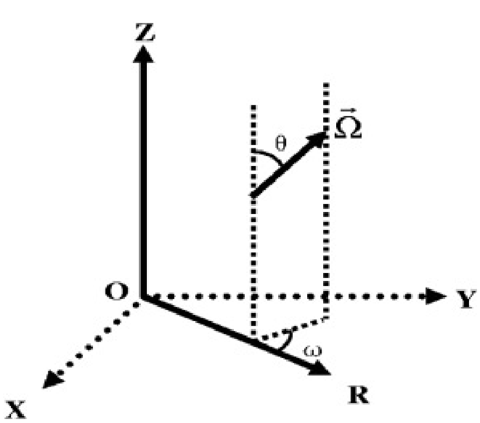

Fig. 1. Directional coordinate system. Here, Ω is the travel direction of photons, θ is the angle of Ω with z axis, and ω is that with the radial direction.

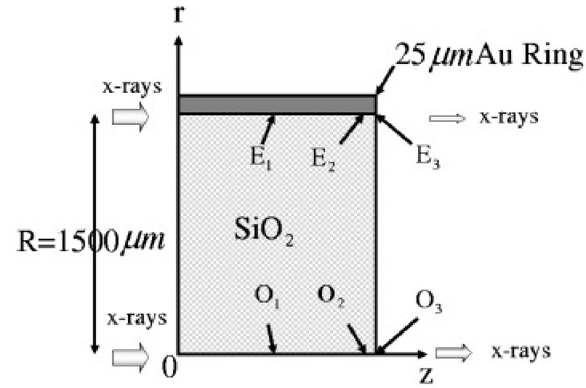

Fig. 2. Schematic of the SiO_2 foam and the Au ring. Here, we define six characteristic positions which are denoted by O_i and E_i $(i = 1,3)$. O_1 and E_1 are in the middle of the foam cylinder; O_3 and E_3 are on the exterior face; and O_2 and E_2 are 50 μm axially away from the exterior face. O_i $(i = 1,3)$ is at the center of the foam cylinder, and E_i $(i = 1,3)$ is at the edge.

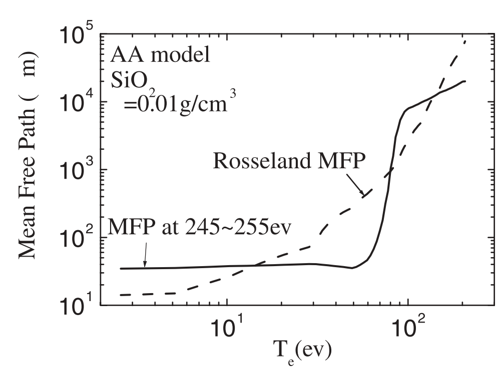

Fig. 3. Temperature dependent mean free path (MFP) at 250 eV and Rosseland MFP in a 10 mg/cm^3 SiO_2.

https://doi.org/10.1017/S026303460505038X Published online by Cambridge University Press

3. SIMULATION RESULTS AND COMPARISON WITH EXPERIMENTS

Because opacity is essential for radiative transfer study, we first compared the opacity obtained by using our average atom model with that given by Back *et al.* (2000*a*). Figure 3 is the temperature dependent mean free path (MFP) at $h\nu =$ 250 eV and Rosseland MFP in a 10 mg/cm^3 SiO_2, obtained by using our average atom model. Here, h is the Planckian constant and ν is the photon frequency. From Figure 3, the MFP at 250 eV is about 40 μm over a wide temperature range, from the cold to 60 eV; and the Rosseland MFP is 230–450 μm over the 40–60 eV. There are some differences between the values above and that given by Back *et al.* (2000*a*). The cold MFP at 250 eV is 40 μm and rises to 50–100 μm at the temperature from 40 to 60 eV, and the Rosseland MFP is 230–550 μm over the 45–60 eV. However, the differences are not remarkable (Back *et al*., 1992).

3.1. Breakout time

Foam emission at $h\nu = 250$ eV with a spectral bandwidth of about 10 eV was measured and its breakout times at the center of the three different length foams were given (Back *et al*., 1992). To compare the simulation results of LARED-R-1 with that measured from the experiments, we choose the spectra range from $h\nu = 245$ eV to 255 eV as a photon group in our simulation. The simulated intensities at $h\nu = 250$ eV vs. time lineouts at O_3 and E_3 of the 0.5, 1.0, and 1.5 mm long SiO_2 foams are shown in Figure 4. As presented, the simulated breakout times t_{bk} at the center of exterior face are 4.7, 7.5, and 10.8 ns for foams of the three different lengths, and are, respectively, 5.2, 8.8, and 12.8 ns at the edge of the foams.

Figure 5 is a radial lineout at 9.5 ns after the X-ray drive started for the 1.0 mm long foams. From Figures 4 and 5, the radiation wave breaks out the center prior to breaking out at the edge, and there is a remarkable curvature in the radiation front. These simulation results agree with Back *et al.* (2000*a*). An analysis was given for the phenomena (Back *et al*., 2000*a*). Here, we just want to emphasize that the energy loss into the heating wall ring is the main reason for the curvature in radiation wave front and breakout timing difference.

In Back *et al*. (2000*a*), experimental data of radial lineout at 9.5 ns and the simulation results by using both detailed OPAL opacity model and an average atom model were presented. Comparing Figure 4 in Schwanda and Eidmann (1992) with Figure 4 here, we can see that simulation results of LARED-R-1 by using average atom model is near the simulation results of Back *et al*. (2000*a*) by using detailed OPAL opacity model, and fit well with the intensity data. The result is quite different from the conclusion made by Back *et al*. (2000*a*), in which it obtained a planar radiation wave front when the average atom model was used in their simulation, and this was imputed to the average atom model in Back *et al*. (2000*a*). Nevertheless, from the simulation results of LARED-R-1, the diffusive approximation plays a more important role in influencing the simulation result than an atomic model, and their simulation result which disagreed with the experiments should be mainly due to the diffusive approximation. We therefore conclude that the multigroup radiation transfer is much more reasonable than the diffusive approximation in simulating the transfer process of the supersonic wave in foam. Moreover, based on the simulation results of Back *et al*. (2000*a*), we can expect a much better simulation result from LARED-R-1 if a detailed OPAL opacity model is used. Our detailed OPAL opacity model is under development, and we will show the simulation results of LARED-R-1 by using the detailed OPAL opacity model in another paper.

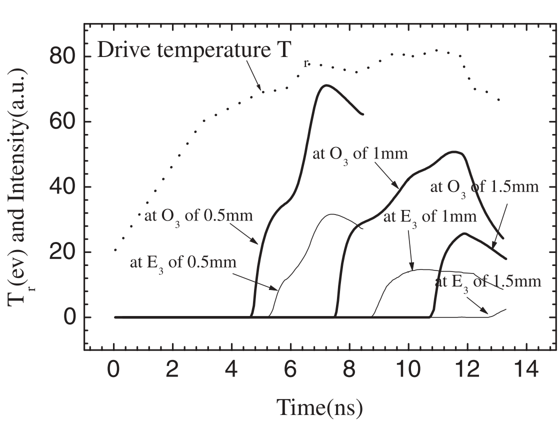

Fig. 4. Simulated intensity at $h\nu = 250$ eV vs. time on O_3 (thick solid lines) and E_3 (thin solid lines) of the 0.5, 1.0, and 1.5 mm long SiO_2 foams. Dotted line is the radiation drive temperature fitted from the experimental result shown in Back *et al*. (2000*a*). The unit of the intensity is arbitrary unit (a.u.), and this is the same in the following figures.

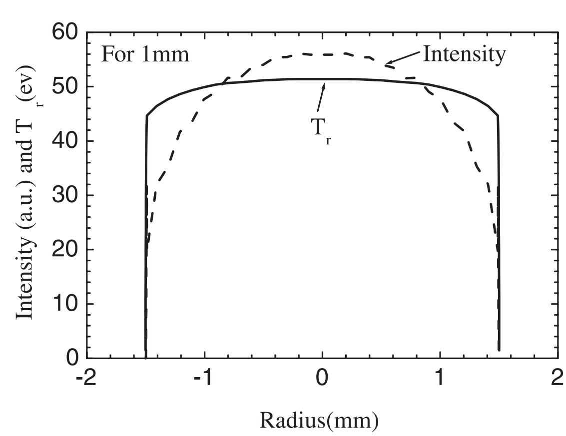

Fig. 5. Simulated T_r and radial lineout of $h\nu = 250$ eV on the center of the exterior face O_3 at the time of 9.5 ns for a 1.0 mm long foam.

3.2. The equivalent radiation temperature T_r and the electron temperature T_e

3.2.1. The radial distribution of T_r on exterior face

We define the equivalent radiation temperature $T_r = (E_r/a)^{1/4}$. Here, E_r is the energy density of radiation and a is the classical radiation constant. We use m to express the mth discrete direction and define $I_{g,m} = \int_{\Delta\nu_g} I_\nu(R, z, \Omega_m, t)\, d\nu$, then we have $E_r = (1/c)\sum_g \sum_m I_{g,m} P_m$. Here, $I_\nu(R, z, \Omega_m, t)$ is the specific intensity at frequency ν as a function of radial position R, axial position z, the mth discrete direction Ω_m and time t. The symbols P_m is the weight for the mth discrete direction and c is the speed of light. The radial distribution of T_r at the exterior face is given in Figure 4. As shown, T_r decreases much slower along the radial direction than the intensity. By using a simple scaling of t_{bk} (Back *et al.*, 2000*a*) and the opacity data from our average atom model, we have $t_{bk} \propto T_r^{-5.2}$. Therefore, t_{bk} changes remarkably although T_r changes little from the center to the edge.

3.2.2. Spatial distribution of T_e and T_r in the R-Z plane

Shown in Figure 6 are spatial distributions of electron temperature T_e and the equivalent radiation temperature T_r in the R-Z plane at the times of 4 ns and 9.5 ns for the 1 mm long foam. As it is shown, T_e is much lower than T_r at the same spatial point at 4 ns, but they are almost the same at 9.5 ns. Furthermore, we can see clearly from Figure 6(a) to 6(d) that there are significant curvatures of T_e and T_r distributions along radial direction.

3.2.3. Relaxation time between T_e and T_r

Figures 7(a) and 7(b) are time evolutions of T_e and T_r on O_1, E_1, O_2, and E_2 of the 1 mm long foam. We define the relaxation time t_{re} as the time when T_e almost equals T_r at the same point, then $t_{re} = 4.7$ ns, 5.3 ns, 7.5 ns, and 8.7 ns on O_1, E_1, O_2, and E_2, respectively. Therefore, t_{re} is shorter at the center than at the edge.

However, the real spectral distribution is far from Planckian distribution even after t_{re}, and more, the angular distribution of the intensity is significantly inhomogeneous, which will be discussed in the following sections. We will use the 1 mm long foam as an example, which is about two Rosseland MFP in length.

3.3. Expansion of Au wall at the source entrance

Expansion of Au wall may make the entrance smaller and obscure the X-ray source. From the simulation results of LARED-R-1, the expansion of the Au wall is insensitive to the length of the foam, and it expands inward about 200 μm at 9.5 ns. This agrees with the experimental results given in Back *et al.* (2000*a*).

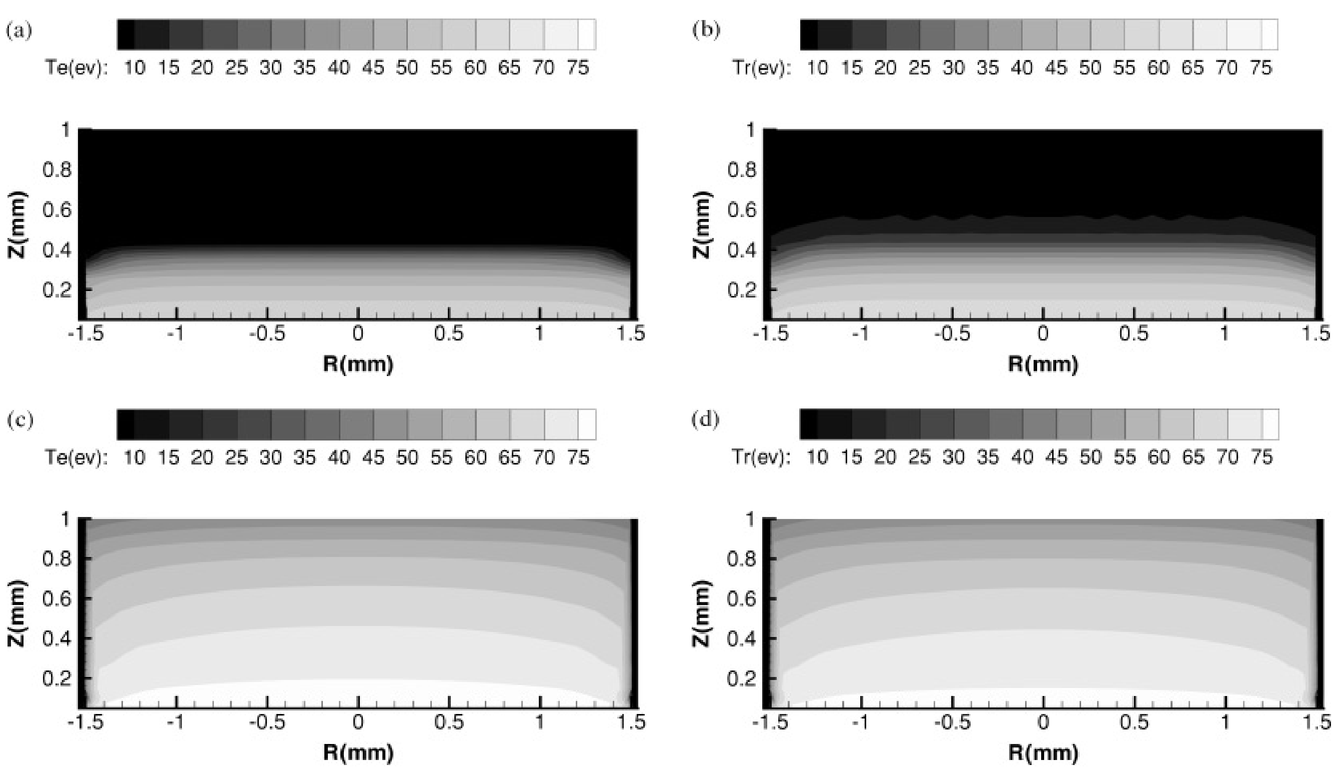

Fig. 6. Spatial distributions of T_e and T_r in R-Z plane at the times of 4 ns and 9.5 ns. (a) T_r at 4 ns; (b) T_e at 4 ns; (c) T_r at 9.5 ns; (d) T_e at 9.5 ns.

https://doi.org/10.1017/S026303460505038X Published online by Cambridge University Press

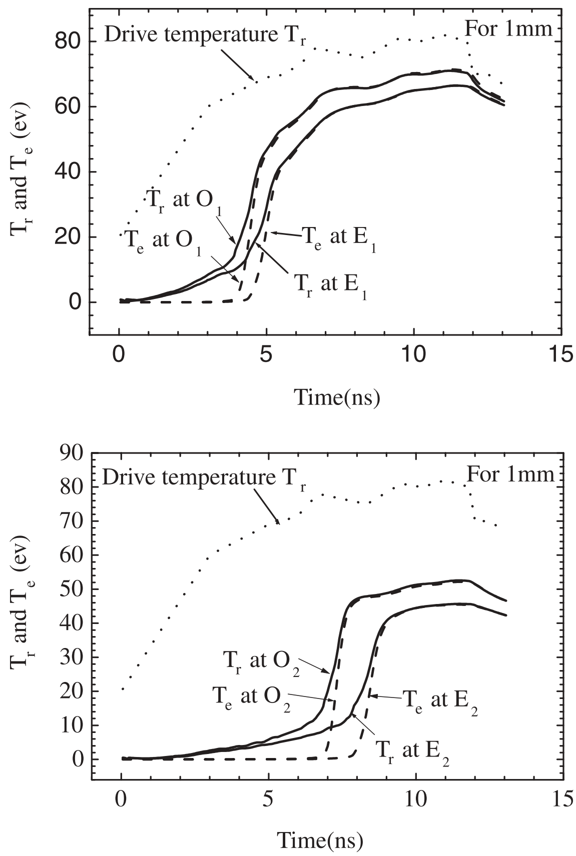

Fig. 7. Temporal electron temperature T_e (solid lines) and the equivalent radiation temperature T_r (dashed lines) on (a) O_1 and E_1, and (b) O_2 and E_2 of the 1 mm long foam. Dotted lines are the radiation drive temperature.

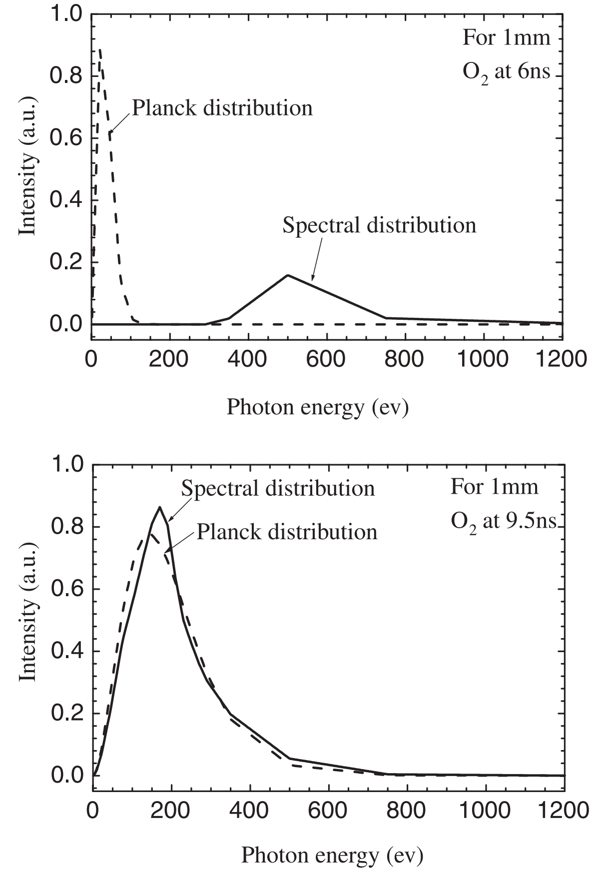

Fig. 8. Comparisons of the spectral distribution (solid line) with Planckian distribution (dashed line) on O_2 of the 1 mm long foam. (a) 6 ns; (b) 9.5 ns. The calculated spectral distribution consists of a sequence of discrete points, each representing the corresponding sum over angles for the corresponding spectral group. The points are not plotted in the figure because the number of spectral groups is large, which is 100. The Planckian distributions have kinks at about $h\nu = 250$ eV and 500 eV, because they are calculated also at those discrete points and the group steps are big at these points. This is the same in Fig. 9.

4. SPECTRAL AND ANGULAR DISTRIBUTIONS

4.1. Spectral distribution

First, we compared the spectral distribution in SiO_2 foam with the blackbody spectral distribution $B_\nu(T_r)$. From Planckian relation, we have $B_\nu(T_r) = (2h\nu^3/c^2)$ $[1/e^{h\nu/(kT_r)} - 1]$. The angular averaged spectral distribution $1/4\pi\Delta\nu_g \sum_m I_{g,m} P_m$ is given by LARED-R-1.

In Figure 8, we present the comparisons of $(1/4\pi\Delta\nu_g)$ $\sum_m I_{g,m} P_m$ with $B_\nu(T_r)$ at times of 6 ns and 9.5 ns at the center point O_2 which is just near the exterior face. As shown, the spectral distribution in SiO_2 is far from the blackbody distribution at 6 ns, but they are near to 9.5 ns. Nevertheless, a remarkable difference still exists even at 9.5 ns.

We further compare $(1/4\pi\Delta\nu_g)\sum_m I_{g,m} P_m$ with $B_\nu(T_r)$ at 9.5 ns at points O_1, E_1, and E_2 in Figure 9. As presented, the spectrum is always harder than the blackbody distribution. The reason for this lies in the fact that the photon with high energy has a longer MFP and is easier to propagate than the photon with lower energy. Moreover, we noticed from Figure 8(b) that the spectral distribution at E_1 is very near the blackbody distribution when we compare it with other points. From Figure 2, E_1 is on the interface between SiO_2 and Au, and it is in the middle of the cylinder. We will see from Figure 10(b) that the radiation at E_1 mainly comes from the Au wall which emission is almost in blackbody distribution.

4.2. Angular intensity distribution in foam

By using S-4 discrete ordinates method to solve the radiative equation of transfer, LARED-R-1 can give the angular intensity distribution in 12 discrete directions for all photon groups. The 12 discrete directions are shown in the figure caption of Figure 10. As shown, θ is 29.7° for $m = 7$ and 10, 69.5° for $m = 8$, 9, 11, and 12, 150.3° for $m = 1$ and 4, and 110.5° for $m = 2$, 3, 5, and 6. Hence, the photon in the directions of $m = 7 - 12$ propagates down the cylindrical foam to the exterior face; while the photon in $m = 1 - 6$ propagates up to the entrance face. On the other hand, $\omega <$ 90° for $m = 4$, 5, 6, 10, 11, and 12, so photons in these

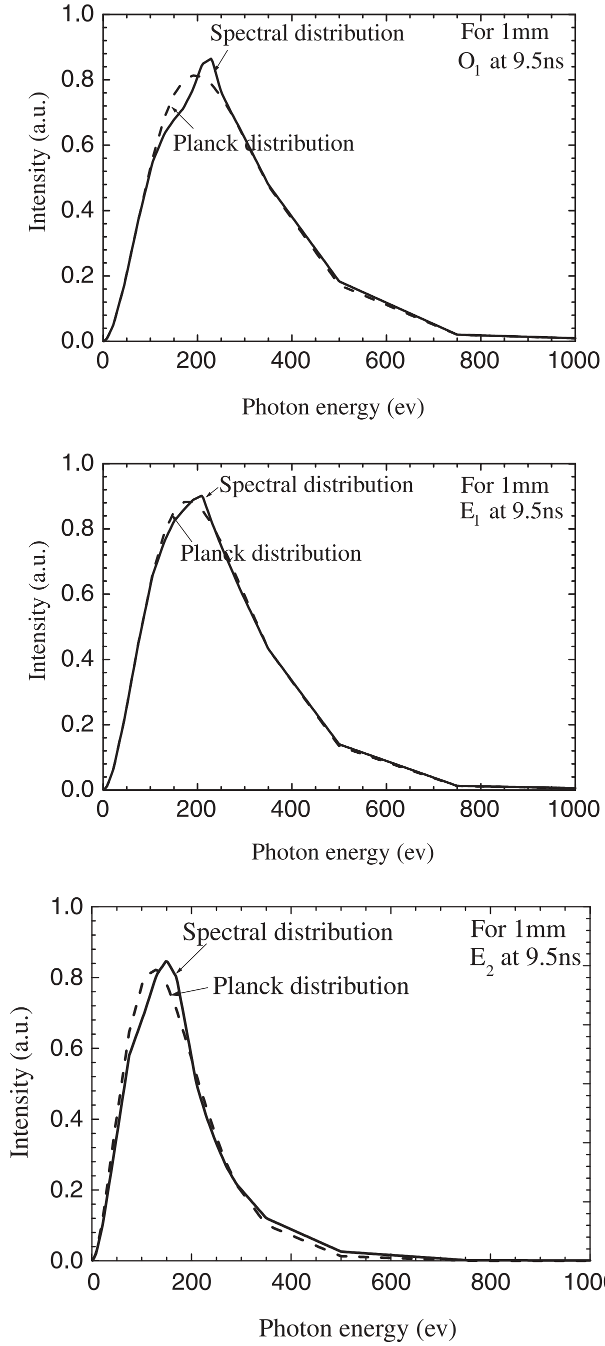

Fig. 9. Comparisons of the spectral distribution (solid line) with Planckian distribution (dashed line) at 9.5 ns on the three characteristic points of (a) O_1, (b) E_1 and (c) E_2. The length of the foam is 1 mm. More explanation of the lines is given in Fig. 8.

directions propagate outward to the Au wall; while $\omega > 90°$ for m = 1, 2, 3, 7, 8, and 9, so photons in these directions propagate toward the inner part of the SiO_2 foam.

Figure 10(a) to 10(d) give the angular intensity distributions at 8 ns, 9.5 ns, and 12 ns, on the center points O_1 and O_2 and at the edge points E_1 and E_2. In Figure 10(d), the intensity distribution at 8 ns is not presented because the emission on E_2 at this time is too weak to be shown. From Figure 10, we can obtain the following conclusions on angular intensity distribution in foam. (1) The intensity is anisotropic throughout the whole foam cylinder, which is two Rosseland MFP in length and three in radius, irrespective of the center, the edge, the middle, or the exterior face. However, it is axis-symmetrically on axis. (2) Emission propagating down ($m = 7 - 12$) is stronger than those up ($m = 1 - 6$) toward the entrance, due to the different boundary conditions on the left and the right of the foam cylinder. It is the X-ray driven source on the left of the foam, while it is the vacuum on the right. Especially at the centers, the emission at $m = 7$ and 10 is the strongest while that at $m = 1$ and 4 is the weakest. This is due to their small angle with the positive or negative z axis, and hence the emission is strongly influenced by the boundary conditions. (3) On centers O_1 and O_2 which are respective one and two Rosseland MFP away from the X-ray entrance, intensity is stronger when θ is smaller. This suggests that the radiations at these points are mainly contributed by transmission of the X-ray source. This is also known from the spectrum at these points, which is harder than the Planckian distribution. Hence, transmission of the X-ray drive in this model, after two Rosseland MFP, is still stronger than re-emission of SiO_2 foam and Au wall.

4.3. Angular intensity distribution on the exterior face

In this part, we further discuss the angular intensity distribution on the exterior face of the foam because it is very important in the measurements. Figure 11(a) and 11(b) are the angular intensity distribution at 250 eV on the center point O_3 and the edge point E_3 on the exterior surface of the 1 mm long foam, at 6, 9.5, and 12 ns. As it is shown, (1) On the center O_3, the angular intensity distribution is axisymmetric and the intensity is stronger when θ is smaller. At 9.5 ns, the radiation in $m = 7$ is 30% stronger than in $m = 8$ and 9. (2) At the edge E_3, it is seriously anisotropic. The intensity in $m = 10$ is more than 12 times stronger than that in $m = 8$ at 9.5 ns. The radiation in $m = 10$, 11, and 12 is mainly the transmission of X-ray source, and that in $m = 7$, 8, and 9 is contributed merely by the re-emission of Au wall. Obviously, the transmission of X-ray source is stronger than re-emission of Au wall.

5. CONCLUSION

The simulation results from the 2D multigroup radiation transfer hydrodynamics code LARED-R-1 agree well with the observations of the supersonic wave experiment done earlier by the Livermore group. However, our simulation shows that, contrary to the conclusion of Back *et al.* (2000*a*), the average-atom opacity model is sufficient to explain the obtained experimental results, provided that an adequate description of the radiation transport was used. Based on the

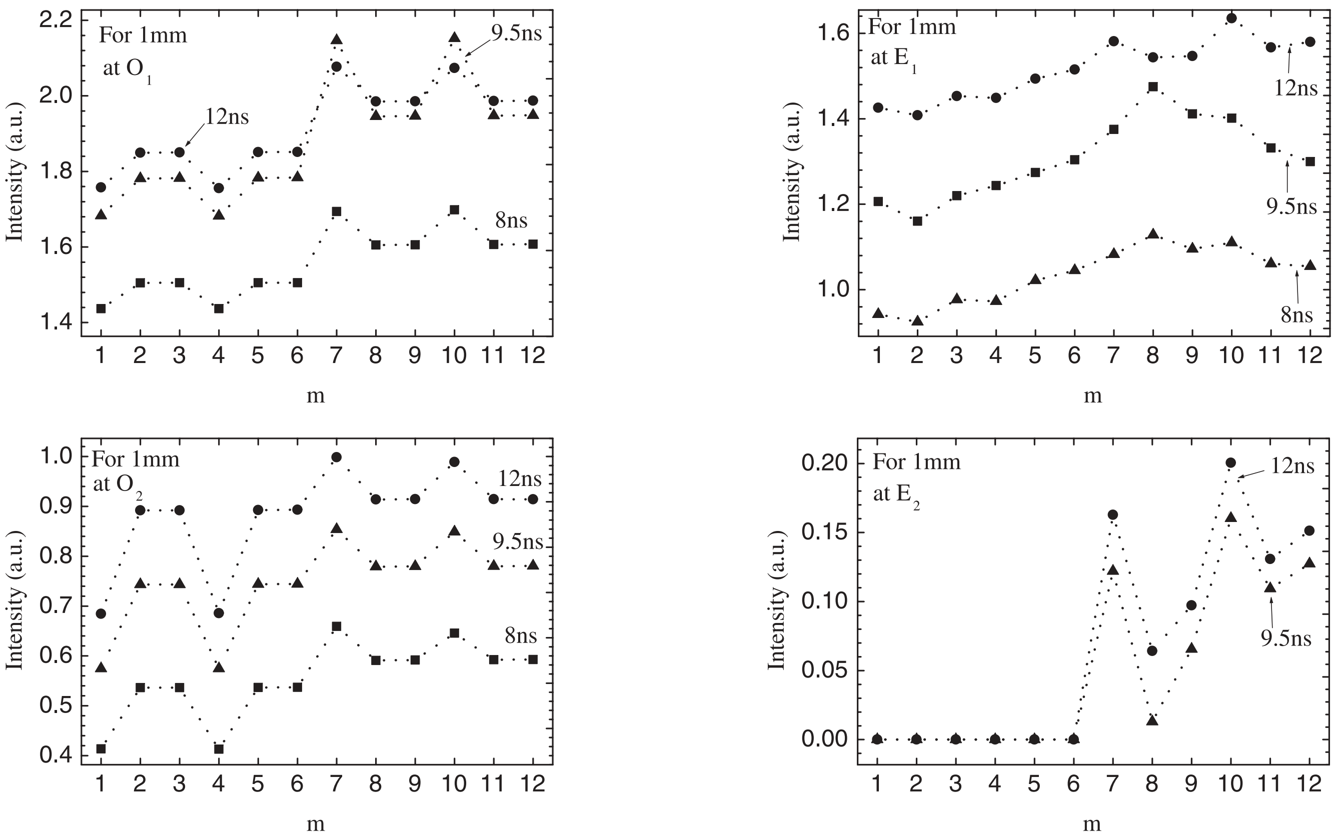

Fig. 10. Angle distributions of the intensity at 8 ns (square), 9.5 ns (triangle), and 12 ns (circle) on the characteristic points of (a) O_1, (b) E_1, (c) O_2 and (d) E_2 of the 1 mm long foam. The (θ, ω) of $m = 1$ to 12 are: (150.3°,135°), (110.5°,158°), (110.5°,112°), (150.3°,45°), (110.5°,68°), (110.5°,22°), (29.7°,135°), (69.5°,158°), (69.5°,112°), (29.7°,45°), (69.5°,68°), (69.5°,22°).

simulations, two important conclusions are obtained. First, the radiation spectrum in the foam is harder than Planckian distribution because the photon of higher energy has a longer MFP. Second, the radiation is anisotropic throughout the whole foam cylinder due to the different boundary conditions on the two cylinder surfaces. This suggests that the diffusive approximation is not suitable for the close investigation of the supersonic wave transfer process in foam. This will be more clear if a comparison between the results from LARED-R-1 and that from a 2D multigroup diffusive radiation transfer code can be made by using the same opacity model. However, we don't have a 2D multigroup diffusive radiation transport hydrodynamics code at present, so this work will be done in the future.

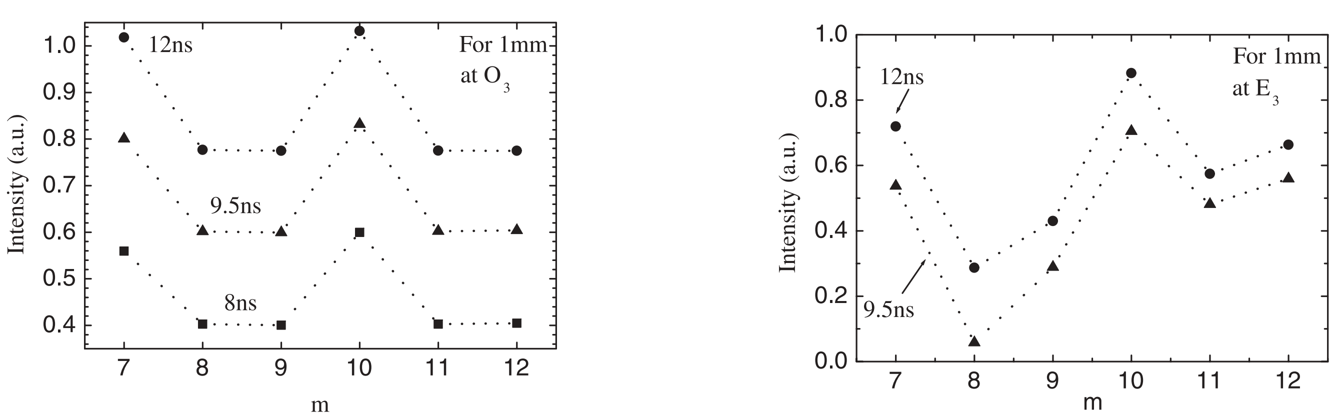

Fig. 11. Angle distributions of the intensity at 8 ns (square), 9.5 ns (triangle), and 12 ns (circle) on the characteristic points of (a) O_3 and (b) E_3 of the 1 mm long foam.

https://doi.org/10.1017/S026303460505038X Published online by Cambridge University Press

REFERENCES

Afshar-rad, T., Desselberger, M., Dunne, M., Edwards, J., Foster, J.M., Hoarty, D., Jones, M.W., Rose, S.J., Rosen, P.A., Taylor, R. & Willi, O. (1994). Supersonic propagation of an ionization front in low density foam targets driven by thermal radiation. *Phys. Rev. Lett.* **73**, 74.

Back, C.A., Bauer, J.D., Landen, O.L., Turner, R.E., Lasinski, B.F., Hammer, J.H., Rosen, M.D., Suter, L.J. & Hsing, W.H. (2000*a*). Detailed measurements of a diffusive supersonic wave in a radiatively heated foam. *Phys. Rev. Lett.* **84**, 274.

Back, C.A., Bauer, J.D., Hammer, J.H., Lasinski, B.F., Turner, R.E., Rambo, P.W., Landen, O.L., Suter, L.J., Rosen, M.D. & Hsing, W.H. (2000*b*). Diffusive, supersonic x-ray transport in radiatively heated foam cylinders. *Phys. Plasmas* **7**, 2125.

Barnard, J.J., Ahle, L.E., Bieniosek, F.M., Celata, C.M., Davidson, R.C., Henestroza, E., Friedman, A., Kwan, J.W., Logan, B.G., Lee, E.P., Lund, S.M., Meier, W.R., Sabbi, G.L., Seidl, P.A., Sharp, W.M., Shuman, D.B., Waldron, W.L., Qin, H. & Yu, S.S. (2003). Integrated experiments for heavy ion fusion. *Laser Part. Beams* **21**, 553–560.

Basko, M.M. & Meyer-ter-Vehn, J. (1993). Hotraum target for heavy ion inertial fusion. *Nucl. Fusion* **33**, 601.

Borisenko, N.G., Akunets, A.A., Bushuev, V.S., Dorogotovtsev, V.M. & Merkuliev, Y.A. (2003). Motivation and fabrication methods for inertial confinement fusion and inertial fusion energy targets. *Laser Part. Beams* **21**, 505–509.

Chaikovsky, S.A., Labetsky, A.Y., Oreshkin, V.I., Shishlov, A.V., Baksht, R.B., Fedunin, A.V. & Rousskikh, A.G. (2003). The K-shell radiation of a double gas puff z-pinch with an axial magnetic field. *Laser Part. Beams* **21**, 255–264.

Feng, T. (1995). Coupling transport diffusion method of calculating radiation transfer in a cavity. *Comp. Phys.* **12**, 375 (in Chinese).

Feng, T., Lai, D. & Xu, Y. (1999). An artificial iteration method for calculating multi-group radiation transfer problems. *Comp. Phys.* **16**, 199 (in Chinese).

Feng, T., Lan, K. & Lai, D. (2001). A comparison between two averaging methods of multi-group parameters in ICF radiation transfer calculation. *Comp. Phys.* **18**, 206 (in Chinese).

Kaiser, N., Meyer-ter-Vehn, J. & Sigel, R. (1989). The X-ray-driven heating wave. *Phys. Fluids B* **1**, 1747.

Lewis, E.E. & Miller, W.F., Jr. (1984). *Computational Methods of Neutron Transport*. New York: Wiley.

Marshak, R.E. (1958). Effect of Radiation on Shock Wave Behavior. *Phys. Fluids* **1**, 24.

Massen, J., Tsakiris, G.D., Eidmann, K., Foldes, I.B., Lower, Th., Sigel, R., Witkowski, S., Nishimura, H., Endo, T., Shiraga, H., Takagi, M., Kato, Y. & Nakai, S. (1994). Supersonic radiative heat waves in low-density high-Z material. *Phys. Rev. E* **50**, 5130.

Menart, J. (2000). Radiative transport in a two-dimensional axissymmetric thermal plasma using the S-N discrete ordinates method on a line-by-line basis. *J. Quant. Spectro. Rad. Transfer* **67**, 273.

Niemann, C., Penache, D., Tauschwitz, A., Rosmej, F.B., Neff, S., Birkner, R., Constantin, C., Knobloch, R., Presura, R., Yu, S.S., Sharp, W.M., Ponce, D.M. & Hoffmann, D.H.H. (2003). Diagnostics of discharge channels for neutralized chamber transport in heavy ion fusion. *Laser Part. Beams* **21**, 13–15.

Philippe, F., Canaud, B., Fortin, X., Garaude, F. & Jourdren, H. (2004). Effects of microstructure on shock propagation in foams. *Laser Part. Beams* **22**, 171–174.

Schwanda, W. & Eidmann, K. (1992). Observation of radiative burnthrough in X-ray heated beryllium by time-resolved spectroscopy. *Phys. Rev. Lett.* **69**, 3507.

Sigel, R., Tsakiris, G.D., Lavarenne, F., Massen, J., Fedosejevs, R., Meyer-ter-Vehn, J., Murakami, M., Eidmann, K. & Witkowski, S. (1990). Experimental observation of laser-induced radiation heat waves. *Phys. Rev. Lett.* **65**, 587.

Zel'dovich, Ya.B. & Raizer, Yu.P. (1966). *Physics of Shock Waves and High-Temperature Hydrodynamic Phenomena*. New York: Academic.